Mutation rates and adaptive variation among the clinically dominant clusters of *Mycobacterium abscessus*

Nicoletta Commins[1], Mark R. Sullivan[2], Kerry McGowen[2], Evan Koch[1], Eric J. Rubin[2,3], Maha Farhat[1,4] *

[1] Department of Biomedical Informatics, Harvard Medical School, Boston, MA, 02115, USA.

[2] Department of Immunology and Infectious Diseases, Harvard T. H. Chan School of Public Health, Boston, MA, 02115, USA.

[3] Department of Microbiology, Harvard Medical School, Boston, MA, 02115, USA.

[4] Division of Pulmonary and Critical Care Medicine, Massachusetts General Hospital, Boston, MA, 02114, USA.

* Correspondence: maha_farhat@hms.harvard.edu

Abstract

Mycobacterium abscessus (*Mab*) is a multi-drug resistant pathogen increasingly responsible for severe pulmonary infections. Analysis of whole genome sequences (WGS) of *Mab* demonstrates dense genetic clustering of clinical isolates collected from disparate geographic locations. This has been interpreted as supporting patient-to-patient transmission, but epidemiological studies have contradicted this interpretation. Here we present evidence for a slowing of the *Mab* molecular clock rate coincident with the emergence of phylogenetic clusters. We find that clustered isolates are enriched in mutations affecting DNA repair machinery and have lower spontaneous mutation rates *in vitro*. We propose that *Mab* adaptation to the host environment through variation in DNA repair genes affects the organism's mutation rate and that this manifests

as phylogenetic clustering. These results inform our understanding of niche switching for facultative pathogens and challenge the model of transmission as the major mode of dissemination of clinically dominant *Mab* clusters.

Introduction

Mycobacterium abscessus (*Mab*) is an emerging, multi-drug resistant pathogen that is increasingly responsible for opportunistic pulmonary disease, most commonly in patients with underlying structural lung conditions such as cystic fibrosis (CF)[1]. *Mab* is divided into three subspecies: *M. a. abscessus*, *M. a. massiliense*, and *M. a. bolletii,* the former two being the most common clinical subspecies[2]. Infections with *Mab* are associated with accelerated decline in lung function and can result in severe disseminated disease and/or loss of eligibility for lung transplantation. *Mab* infections are difficult to treat, requiring a prolonged antibiotic regimen with high rates of treatment failure[3].

Until recently, *Mab* infections were thought to be acquired independently by each patient from environmental reservoirs in soil or water. Large scale analyses of whole genome sequencing (WGS) of Mab clinical isolates have revealed that a large proportion of clinical isolates fall into several phylogenetically characterized clusters, often termed dominant circulating clones[4]. Isolates within these clusters have high core genome similarity that is not explained by point source outbreaks as they were sampled from diverse geographic origins. These observations have been interpreted as supporting widespread recent transmission, either through direct contact or indirectly through fomites, but a number of epidemiological studies have refuted person-to-person transmission as a major mode of *Mab* dissemination[5–11]. Reconciling these conflicting lines of evidence is important as they dictate public health practice and allocation of resources to protect vulnerable populations from infection. However, it is still unclear what role transmission plays in the emergence of *Mab* clusters.

While widespread transmission is one proposed explanation for the phylogenetic structure observed in *Mab*, it is important to consider other factors in the species' evolutionary history that may contribute. For example, transient niche switching between environmental sources and the human host may introduce bottlenecks resulting in low diversity and effective population size. Another explanation is a change in mutation rates, either through changes in bacterial generation time or through genetic variation. A third consideration is clinical sampling, where particular *Mab* lineages that cause more frequent, severe and/or persistent disease are more likely to be isolated and sequenced. Consistent with the latter hypothesis, previous work has shown that isolates within clusters are more likely to contain point mutations associated with antibiotic resistance and are associated with greater bacterial burden and lung inflammation in mice[4].

Interpreting tree structures in the context of population history is aided by phylogenetic dating, which translates genetic distances into time scale. Previous studies[4,9,12,13] have estimated molecular clock rates in *Mab* but these have been limited to subpopulations within clusters. Here we report on molecular clock rate estimation for the deep branches of the *M. a. abscessus* phylogeny and for within-host isolates belonging to clusters. We provide evidence for an evolutionary slow-down coincident with the expansion of clinically dominant clusters and propose that the emergence of dense phylogenetic clustering in *Mab* may result from genetically encoded changes to the mutation rate. These results indicate that transmission is not the only plausible explanation for the dense clustering observed in the *Mab* phylogeny, and that more research is needed to clarify the transmission dynamics of this emerging pathogen.

Results

<u>Phylogenetic analysis confirms the presence of large, dominant clusters (DCs) spanning multiple geographies</u>. We identified 1,629 *M. abscessus* isolates with publicly available whole genome sequencing (WGS) data and associated dates of collection (Table S1). We excluded isolates with

76 likely contamination or low-quality assemblies (Methods). Among the 1,461 isolates passing
77 quality filters, the majority (80.1%) were derived from *in vitro* culture of pulmonary samples (Table
78 S2). Of the 1,181 pulmonary isolates, 98.3% (1,161/1,181) were collected from patients with cystic
79 fibrosis (CF), while the rest were collected from patients with no documented diagnosis. The
80 dataset represented 483 patients with unique patient identifiers, with 59.6% (288/483) of patients
81 contributing a single isolate, and the remaining contributing between 2 to 24 isolates sampled
82 over time. Isolates originated from nine countries and were collected between 1998-2017, except
83 for the reference strain ATCC 19977 which was collected in 1957 (Figure 1B).

84 The majority (91.7%) of samples had ≥98% average nucleotide identity (ANI) with one of
85 three reference genomes (Table S3) representing each of the three Mab subspecies, consistent
86 with the commonly used ANI threshold for bacterial subspecies. Isolates with <98% ANI with any
87 subspecies were excluded from downstream analysis. The resulting dataset overrepresented
88 clinically relevant subspecies of *M. abscessus*, with 93.9% belonging to either *M. a. abscessus*
89 or *M. a. massiliense*. To better resolve true evolutionary relationships among samples, we defined
90 and restricted analysis to the core genome for each subspecies, then further excluded predicted
91 recombination events (Methods). We performed maximum likelihood (ML) phylogenetic analysis
92 for each of the three *Mab* subspecies, using only the first isolate from each patient to focus on
93 between-host diversity. The resulting subspecies trees confirmed the presence of multiple,
94 globally distributed clades with dense phylogenetic clustering (Methods). We excluded clustering
95 due to potential point source outbreaks by limiting to clusters containing isolates from more than
96 one country and a minimum of three isolates for downstream analysis. In total, we confirmed 16
97 clusters (Figure S2A) including four clusters with > 50 isolates, which we refer to here as dominant
98 clusters (DCs). Isolates within clusters comprised 76.4% of isolates included in the phylogenetic
99 analysis. The median pairwise distance in *M. a. abscessus* DC 1 was 68 SNPs. For comparison,
100 the mean pairwise distance across the subspecies trees were 5537, 4100, and 8034 SNPs for *M.*
101 *a. abscessus*, *M. a. massiliense*, and *M. a. bolletii*, respectively. All four DCs contained isolates

102 originating from three continents (North America, Europe, and Australia). Clustered isolates also
103 spanned the full range of isolation times, including ATCC 19977, which was placed within *M. a.*
104 *abscessus* DC 1 despite having been collected at least 40 years before any other isolates in the
105 tree (Figure 1A-B).
106
107 Coalescent analysis reveals a faster long-term evolutionary rate than observed in DCs. To aid in
108 transmission inference and to reconstruct the evolutionary history of *Mab*, we performed a
109 coalescent analysis using our SNP alignment. Previous work has reported molecular clock rates
110 within *Mab* clusters, but to our knowledge no study has successfully dated any of the full *Mab*
111 subspecies phylogenies. To evaluate the presence of temporal signal, we performed root-to-tip
112 regression for each subspecies tree but in each case did not observe a positive correlation
113 between sampling date and root-to-tip distance. We reasoned that the high degree of dense
114 clustering in the *Mab* phylogeny may obscure the genetic-temporal signal. To test this hypothesis,
115 we pruned each subspecies tree until it contained the minimal number of samples required to
116 capture 95% of the genetic diversity in the original tree (Methods). Following pruning of the *M. a.*
117 *abscessus* subspecies tree, root-to-tip regression demonstrated the presence of temporal signal
118 (Figure 1C, D). Evidence of temporal signal in *M. a. abscessus* was further strengthened using a
119 permutation test and a Bayesian evaluation of temporal signal (Figure S2C, Table S4).
120 We used a Bayesian implementation of coalescent analysis, BEAST[14], to estimate the
121 molecular clock rate of the pruned *M. a. abscessus* subspecies tree assuming a relaxed clock
122 model, which allows each branch of the tree to have its own clock rate. To explore the effect of
123 the tree prior on molecular clock estimation, we ran analyses using two different tree priors,
124 assuming either a constant coalescent model, which assumes constant population size over time,
125 or a Bayesian skyline coalescent model, which allows the population size to change over time.
126 While the Bayesian skyline coalescent had a slightly better marginal likelihood, we found no
127 significant difference between the clock rates estimated by the two models (Table 1, Figure 2C).

128 Our estimates for the clock rate in the long, internal branches of the tree were approximately 10-
129 fold faster than nearly all previously reported estimates of the clock rate within *Mab* clusters
130 (Figure 2C). The clock rate estimate we obtain is sensitive to which samples are selected by
131 Treemmer (Figure S3C). We therefore performed multiple runs using independent sets of isolates
132 sampled by Treemmer and present the most conservative estimate we obtained from Treemmer
133 sampling. Clock rate estimates were also robust to the algorithm choice or stringency of the
134 recombination search procedure (Figure S3B). We next attempted to date the full (unpruned) *M.*
135 *a. abscessus* phylogeny using the faster rate inferred from our coalescent analysis of the pruned
136 tree. These chains suffered from poor convergence and sampled trees with a distorted topology,
137 elongating the short branches and eliminating the densely clustered structure observed in the ML
138 phylogeny (data not shown). We therefore hypothesized that the lack of temporal signal in the full
139 *M. a. abscessus* dataset may result from a difference between the long-term clock rate and the
140 more recent evolutionary rate within phylogenetic clusters.
141
142 Analysis of longitudinally sampled within-host isolates supports a slower clock rate in DCs. To
143 further investigate the differences in clock rate between long-term historical time scales and short-
144 term contemporary time, we used pairs of isolates sampled from the same patient over time to
145 estimate the mutation rate. We focused on estimating a within-host clock rate for *M. a. abscessus*
146 to compare directly with the estimate from our coalescent analysis and because we had the most
147 longitudinal samples for this subspecies. All isolate pairs belonged to one of the *M. a. abscessus*
148 DCs. Because polyclonal *Mab* infection is common in CF patients, we first excluded any isolate
149 pairs with a SNP distance > 20. This threshold was selected by comparing the distribution of all
150 possible within-host isolate pairs to the distribution of pairwise SNP distances within *Mab* DCs
151 (Figure 2A, Figure S4). Regressing the SNP distance between isolate pairs on the time between
152 sample pairs yielded a mutation rate of 2.21 SNPs/year [1.06 – 3.37 95% CI], or 5.17×10^{-7}
153 SNPs/site/year [2.48×10^{-7} – 7.92×10^{-7} 95% CI]. This value is more similar to previously reported

154 molecular clock rate estimates within *Mab* clusters[4,9,12,13] than to those estimated in the long
155 branches of the phylogeny (Figure 2C).
156
157 Simulated ancestries support mutation rate slow-down over population size effects as the major
158 driver of phylogenetic clustering. To test whether sampling from clades with low genetic diversity
159 is sufficient to explain the degree of clustering observed in the ML phylogeny, or whether changes
160 in the molecular clock rate are a better explanation for the observed phylognetic data, we
161 performed coalescent simulations of ancestries with one clustered subpopulation (A) and one
162 unclustered subpopulation (B). Under a range of effective population sizes (N_e) and mutation rates
163 (μ), we simulated ancestries through time with 1000 replicates per simulation. For each replicate
164 we assessed the degree of phylogenetic clustering by measuring d_A/d_B where d_i is the mean
165 pairwise SNP distance within subpopulation i. The total N_e (N_e^T), number of samples, and
166 sampling dates for subpopulations A and B were drawn from the true values for *M. a. abscessus*
167 DC 1 and from all "unclustered" isolates in our dataset, respectively (Figure 3A). We first tested
168 whether a smaller population size for the clustered subpopulation A (N_e^A) could explain the degree
169 of phylogenetic clustering observed. We estimated a range of realistic values for N_e^A using BEAST
170 by assuming a range of possible clock rates (Table S5). These rates spanned a published clock
171 rate estimate for *M. a. abscessus* DC1 to a clock rate that is 50-fold higher, far exceeding the
172 upper 95% highest posterior density (HPD) interval for the published value[15,16]. A schematic
173 outlining this procedure is available as Figure S5. Under the the simulated conditions of equal
174 mutation rates between subpopulation A and B, we only observed phylogenetic clustering to the
175 extent observed in the clinical isolate phylogeny in the scenario where $N_e^T >> N_e^A$ (Figure 3B,
176 Figure S6). We next tested whether a change in the mutation rate at the root of supopulation A
177 could better explain the observed phylogenetic structure in *Mab*. The simulated ancestries where
178 N_e^A and N_e^B are fixed and the mutation rate slowdown is between 10- and 20-fold recapitulated
179 the observed phylognetic structure (Figure 3C). This result was robust to changes in N_e^A and N_e^T

180 across the 95% HPD for each parameter (Figure S7). These results indicate that for person-to-
181 person transmission to drive phylogenetic clustering in *Mab*, the total N_e must be very large
182 compared to the N_e of the clustered subpopulation, an unlikely scenario given the observed
183 genetic data and sampling times. By contrast, a mutation rate change of 10- to 20- fold explains
184 the degree of clustering observed in *Mab* under more realistic population sizes given these data.
185
186 UvrD/Rep family helicases are enriched in DCs in *M. a. abscessus*. To identify genetic variants
187 under positive selection in *Mab* clusters, we searched for evidence of phylogenetic convergence
188 in the core genome of *M. a. abscessus* with regions of recombination excluded. Briefly, we
189 performed ancestral sequence reconstruction for the internal nodes of the subspecies tree and
190 counted the number of independent arisals of each SNP (Methods). Of the 65,202 SNPs identified
191 in *M. a. abscessus*, 34,813 (53.4%) of mutations occurred only once and were excluded. For the
192 remaining SNPs, we ranked each by its enrichment in DCs relative to other regions of the *M. a.*
193 *abscessus* tree (Figure 4A). The most significantly enriched variants in the *M. a. abscessus* DCs
194 included homologs of several known or putative virulence factors as well as a number of cluster-
195 enriched mutations in UvrD-like helicases *MAB_1054*, *MAB_3515c*, and *MAB_3516c* (Figure 4A,
196 Table S6). While the function of these genes is not well characterized in *M. abscessus*, all three
197 genes share homology with the UvrD/Rep family of helicases. This family of genes is involved in
198 DNA repair and has been associated with growth and persistence *in vivo*[17].
199
200 Isolates in *Mab* DCs are associated with a lower spontaneous mutation rate. To test the
201 association between phylogenetic clustering and spontaneous mutation rate, we selected *M. a.*
202 *abscessus* and *M. a. massiliense* strains that were grouped within DCs or that were not present
203 in those clusters. Each of the strains present in the DCs has the derived (minor) allele at four sites
204 in the UvrD/Rep family genes *MAB_1054*, *MAB_3515c*, and *MAB_3516c*, and the strains outside
205 of DCs possess the ancestral (major) allele at those sites (Table 2, Figure 4A). The strains used

206 and their genotypes are described in Tables S7. The spontaneous mutation rate was estimated
207 in all strains using a fluctuation assay[18] adapted for use in *M. abscessus*. The fluctuation assay
208 counts cells gaining resistance to the antibiotic amikacin during growth in culture without antibiotic.
209 By normalizing the number of mutational events to the population size of the culture, the
210 fluctuation assay estimates the spontaneous mutation rate per generation per the number of
211 bases that can be mutated to confer resistance to amikacin. The strains chosen display similar
212 growth rates (Figure S8A) and very low baseline resistance to amikacin (Table S8) which allows
213 them to be compared using a fluctuation assay. Among *M. a. abscessus* strains, those present in
214 DCs with the derived (minor) allele at the four UvrD/Rep loci had lower spontaneous mutation
215 rates than those with the ancestral (major) allele (Figure 4C). A similar trend was observed in *M.*
216 *a. massiliense* strains (Figure 4D). Further, the average mutation rate was significantly lower in
217 isolates present in DCs across both subspecies (Figure 4E), consistent with the hypothesis that
218 the emergence of dense clustering may be driven in part by changes in mutation rate.
219

220 **Discussion**

221 In this study we have pooled a large global sample of *Mab* genome sequences and
222 examined evolutionary rates and positive selection with the goal of understanding the emergence
223 of *Mab* clusters. We present evidence supporting a slower evolutionary rate within DCs compared
224 to the long internal branches of the phylogeny and further data associating genetic variation in
225 DNA repair genes with the slower evolutionary rate. We posit that changes to the mutation rate
226 underlie the dense clustering in *Mab*, and that while other effects such as population or
227 transmission bottlenecks and sampling bias may contribute to the low genetic diversity within
228 clusters, they are not sufficient to explain the observed phylogenetic structure given the available
229 data.

230 Previous studies have restricted molecular clock rate estimation to *Mab* clusters, most
231 likely because of the lack of temporal signal at the subspecies-level. By pruning the *Mab* tree

232 while preserving the majority of the subspecies diversity, we were able to measure a molecular
233 clock rate for *Mab* spanning the time scale from the common ancestor of the subspecies to the
234 present. Estimates of evolutionary rates are recognized to depend on the time scale of
235 measurement. In such examples, the clock rate usually decreases with increasing time depth[18].
236 We observe the opposite effect where the clock rate increases with time depth. The pruned *Mab*
237 tree most likely reflects an evolutionary process taking place predominantly in environmental
238 reservoirs, in contrast to phylogenetic clusters where terminal branches reflect evolution within
239 the human lung environment. We also note that our measurement of within-host mutation rate in
240 *Mab* was independent of phylogenetic inference and the full temporal signal in our sample.
241 Nevertheless, the measured rate within-host was comparable to the clock rate measured
242 previously using coalescent analysis within clusters (Figure 2C).

243 The molecular clock rate is influenced by both the spontaneous mutation rate and the
244 generation time of an organism. Changes in generation time could result from physiological
245 constraints of the human lung environment, if for example, differences in nutrient availability
246 change the growth rate in the lung compared to those living in environmental reservoirs.
247 Generation times and spontaneous mutation rates can also be modified by genetic changes, for
248 example to DNA replication or repair machinery. The observation that some lineages have
249 acquired phenotypes that are beneficial in the host environment[4] raises the possibility that genetic
250 changes that underlie or associate with this adaptation affect mutation rate, either directly by
251 affecting DNA replication or repair machinery, or indirectly by affecting the growth rate. Ruis et al.
252 reported differences in mutational signatures along internal branches of the subspecies phylogeny
253 compared to internal branches of DCs, supporting a change in the mutational process within some
254 clades of the tree[19].

255 We scanned the core genomes for variants enriched in the DCs in *M. a. abscessus*, the
256 subspecies for which we have the most WGS data and for which there are the highest number of
257 clusters. Notably, we observed several cluster-enriched mutations in UvrD-like helicases. UvrD is

258 a superfamily 1 helicase that is involved in DNA repair and is widely conserved in gram-negative
259 bacteria. UvrD1 in *M. tuberculosis* plays an important role both in nucleotide excision repair (NER)
260 and in pathogenesis and persistence because its DNA repair activity confers tolerance to reactive
261 oxygen intermediates (ROI) and reactive nitrogen intermediates (RNI)[20]. Mutations that promote
262 the activity of UvrD1 and its homologs may therefore increase resistance to genotoxic stress in
263 the context of the human lung environment, with the additional consequence of decreasing the
264 spontaneous mutation rate. We also observed mutations in UvrD-like helicases occurring along
265 the cluster-defining branch of the large *M. a. massiliense* cluster, further supporting the role of the
266 NER pathway in *Mab* pathogenesis.

267 Our study has several limitations. Our dataset overrepresented clinical isolates from the
268 UK where routine whole genome sequencing is part of *Mab* surveillance. Oversampling of some
269 lineages and geographies may mean that we have not adequately captured the global *M.*
270 *abscessus* diversity and that we may have focused on large phylogenetic clusters because of
271 their geographic distribution and not because of their clinical significance. While our results
272 support a faster molecular clock rate in the long internal branches of the phylogeny compared to
273 clustered lineages, we are unable to distinguish between rate differences due to the spontaneous
274 mutation rate from generation time effects. Differences in growth conditions across environments
275 is difficult to quantify as *Mab* is ubiquitous in both natural and built environments, but nutrient
276 availability likely differs greatly between natural reservoirs such as soil and water compared to
277 man-made reservoirs such as showerheads. A healthy lung supports relatively little bacterial
278 growth, but inflammation increases nutrient availability by promoting mucus production and
279 vascular leakage into the airway[21]. Our analysis of variants associated with phylogenetic
280 clustering is also limited in its ability to identify true causal genotypes or those that are enriched
281 in clusters due to hitchhiking to other adaptive variants.

282 It is possible that our recombination removal procedure does not detect every mutation
283 imported by recombination, and that unpurged recombination events may contribute to the high

clock rate we measure in the pruned phylogeny. We believe any effect of recombination is likely minimal for several reasons: 1) recombination rates vary widely across branches, making unpurged recombination events more likely to erode temporal signal than to cause a systematic error in clock rate estimates (Figure S2A), and 2) our clock rate estimates were robust to choice of algorithm or to the stringency of recombination search (Figure S2B. Moreover, the algorithms we used to purge recombination events were also used in previous studies that published *M. abscessus* phylogenies.[4,9,12,13] If these algorithms fail to purge enough recombination events to result in extreme distortion of clock rate estimates, they must also create distortion in phylogenies and the inference that follows from them. This strengthens the argument that phylogenetic clustering is not sufficient to infer widespread transmission.

While our study argues against transmission as the main driver of *Mab* dissemination and the emergence of DCs, these findings do not address the geographic distribution of Mab within clusters. It is possible that DC-associated variants such as the UvrD/Rep mutations described in this study are acquired ancestrally to the emergence of each DC, then circulated via contaminated household or medical equipment. This is similar to the model proposed by Bryant and colleagues, in which variation acquired along the branches ancestral to DCs creates large phenotypic changes, conferring a sudden increase in intracellular survival, tolerance to nitric oxide, and amikacin resistance.[23] It is likely that emergence of clades with higher virulence potential involves acquisition of multiple genotypes including core genome mutations and horizontal gene transfer. Convergent evolution can also act in concert with the Bass Becking hypothesis that “everything is everywhere but the environment selects.” This could generate DCs that have a common core genome across many genetic loci and are prevalent in human infection across a wide range of geographies. Currently there is little publicly available sequencing data from environmental isolates. Isolating and sequencing *M. abscessus* from the environment could aid in understanding why clustered *Mab* isolates are detected in distant geographic locations. Future work could also compare genotypes and mutation rates in environmental samples compared to clinical isolates.

310 In summary, we present new evidence for changes in the molecular clock rate that
311 contribute to the dense phylogenetic clustering observed in *Mab*. These results argue against
312 person-to-person transmission as the primary driver of clustering in the *Mab* phylogeny.
313 Continuing genomic surveillance is needed to understand how *Mab* may be adapting to human
314 infection and to characterize the risk of transmission to at-risk patients. We argue further that the
315 phylogeographic structure of *Mab* is influenced by its complex ecological history as an emerging
316 facultative pathogen that should be considered carefully in future analysis of *Mab* genomic data.
317 Future work should extend these analyses by examining differences in mutation rates and
318 phenotypes between clinical isolates and environmental strains for evidence of host adaptation.
319

320 **Acknowledgements**

321 We thank members of the Farhat lab for feedback and discussion. We are grateful to Luca Freschi
322 for advice on processing WGS data, calling variants, and phylogenetic inference; Maximillian
323 Marin for input on calculating mappability pileup; and Roger Vargas for support in homoplasy
324 counting. We also thank Wilder Wohns for discussions on implementing ancestry simulations with
325 mutation rate changes through time. M.R.S. is a Merck Fellow of the Damon Runyon Cancer
326 Research Foundation, DRG-2415-20. Computational resources and support were provided by the
327 Orchestra High Performance Compute Cluster at Harvard Medical School, which is funded by the
328 NIH (NCRR 1S10RR028832-01).
329

330 **Author Contributions**

331 Conceptualization, N.C. and M.F.; Methodology – Computational analysis, N.C., E.K., and M.F.;
332 Methodology – Experimental studies, M.R.S., K.M.; Investigation – Computational analysis, N.C.;
333 Investigation – Experimental studies, M.R.S., K.M.; Data Curation, N.C.; Writing – Original Draft,
334 N.C. and M.R.S.; Writing – Review & Editing, N.C., M.R.S., E.K., M.F.; Supervision, E.J.R., M.F.
335

Declaration of Interests

The authors declare no competing interests.

362 **Tables**

363

364 **Table 1**. Coalescent analysis results and model comparison

Model	**Marginal Log Likelihood (SD)**	**UCLD Rate (SNPs/site/year)**	**UCLD St. Dev.**
Coalescent constant population	-7144301.64 (21.42)	2.82×10^{-6} [1.33×10^{-6}, 4.83×10^{-6}]	0.182 [0.135, 0.234]
Bayesian skyline coalescent	-7144118.76 (19.93)	2.63×10^{-6} [1.16×10^{-6} , 4.0×10^{-6}]	0.181 [0.138, 0.232]

365

366
367
368
369
370
371
372
373
374
375
376
377
378
379
380
381
382
383
384
385
386
387
388
389
390
391
392
393
394
395
396
397
398
399
400

Table 2. Summary of top 10 nonsynonymous variants enriched in DCs of *M. a. abscessus*

Gene	Gene Symbol	Description	Comments	Enrichment p-value (FDR adjusted)	Number of clustered taxa containing variant	Number of unclustered taxa containing variant
MAB_3334c	*gatB* [c]	Aspartyl/glutamyl-tRNA (Asn/Gln) amidotransferase subunit B [c,d]	Essential for growth and survival *in vivo* in *M. tuberculosis* [17]	6.70×10^{-62}	240	1
MAB_3244		Mercury resistance transport protein/cytochrome c biogenesis protein [c]		5.56×10^{-61}	189	3
MAB_3480		Putative short chain dehydrogenase/ Reductase [c]		1.55×10^{-60}	232	13
MAB_4141 [a]		PE/PPE family protein [c]		1.70×10^{-59}	189	2
MAB_3242	*fni* [c]	Isopentenyl-diphosphate delta-isomerase [c,d]		7.47×10^{-59}	189	3
MAB_3481	*fadE* [c]	Probable acyl-CoA dehydrogenase [c]	FadE mutations in *Mtb* result in decreased growth and virulence in macrophages and in mice[18]	1.69×10^{-58}	232	15
MAB_4057c	*mshA* [c]	D-inositol 3-phosphate glycosyltransferase [d]	Catalyzes biosynthesis of mycothiol, an important compound in resisting oxidative stress and detoxifying harmful agents such as antibiotics[19]	1.80×10^{-57}	189	2
MAB_3581c		Hypothetical protein		3.59×10^{-57}	169	3
MAB_1054 [b]	*pcrA* [c] / *uvrD1* [d]	ATP-dependent DNA helicase [c,d]	Involved in nucelotide excision repair (NER), mismatch repair (MMR), homologous recombination (HR), and rolling circle replication[15]	1.45×10^{-55}	216	7
MAB_3515c	*rep* [c,d]	ATP-dependent DNA helicase [c,d]	Involved in NER, MMR, HR and rolling circle replication[15]	1.46×10^{-55}	189	7

452 **Table 2 Legend:**
453 [a] Multiple variants in *MAB_4141* have been collapsed and the lowest p-value is shown. See
454 Supplementary Material for full list of homoplasic SNPs ranked by their enrichment in clusters.
455 [b] Gram-negative bacteria possess UvrD and a closely related homolog, Rep, while gram-positive
456 bacteria possess a single homolog called PcrA.[24]
457 [c] Mycobrowser annotation
458 [d] prokka annotation
459
460
461
462
463
464
465
466
467
468
469
470
471
472
473
474
475
476
477
478
479
480

481 **Figures**

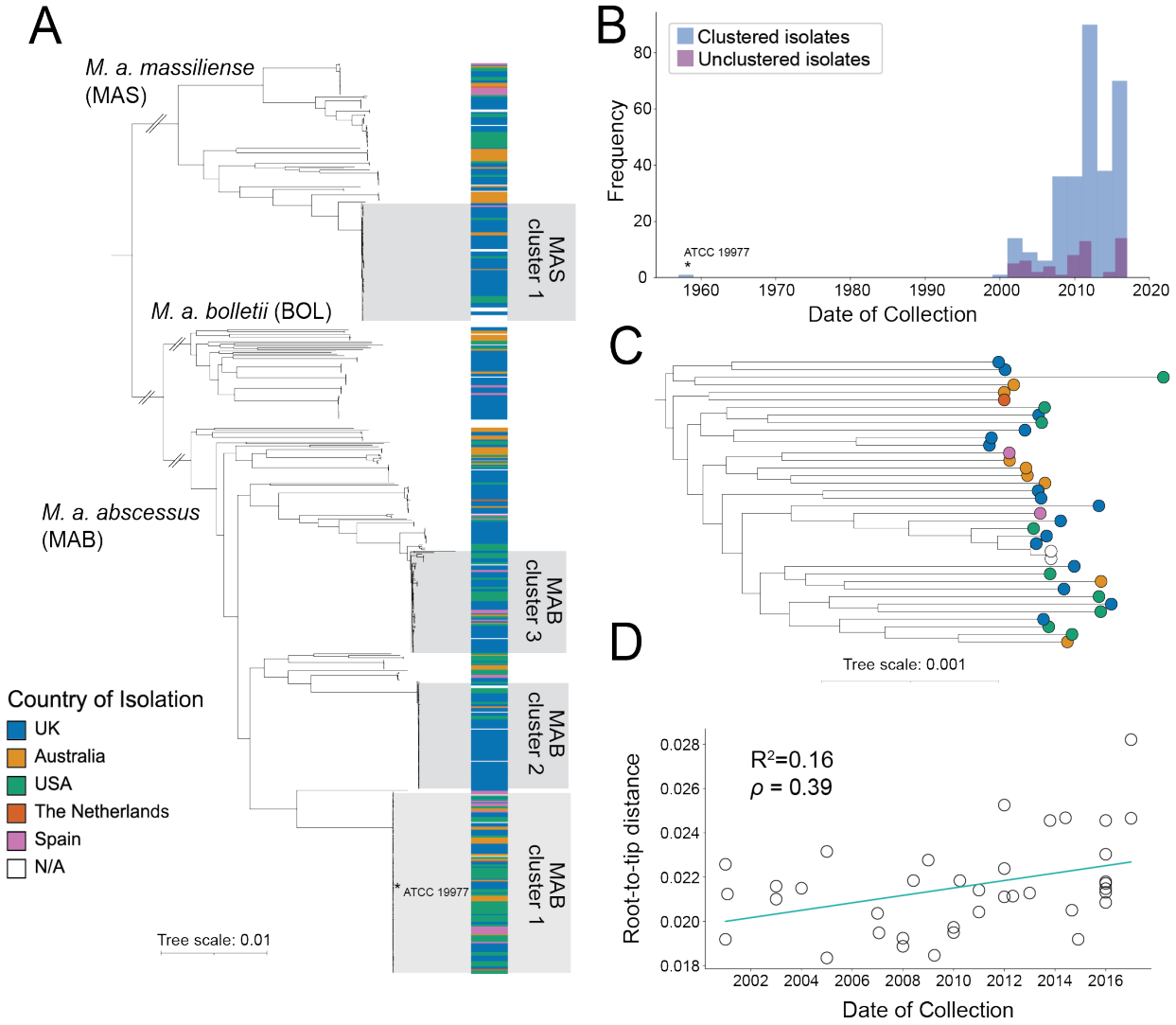

482

483 **Figure 1. Dominant clusters of *M. abscessus* and the presence of temporal signal in**
484 **internal branches.** A) Species-wide phylogeny of *M. abscessus* representing one isolate per
485 patient to avoid within-patient clustering of samples. Each subspecies tree was constructed
486 independently using a subspecies specific reference genome. The four largest phylogenetic
487 clusters are highlighted. B) Histogram showing the distribution of collection dates of all clustered
488 isolates v. all unclustered isolates in *M. a. abscessus*. C) Pruned *M. a. abscessus* phylogeny
489 representing 95% of the original subspecies tree diversity. C) Root-to-tip regression showing
490 evidence of positive temporal signal in the pruned tree shown in (B).

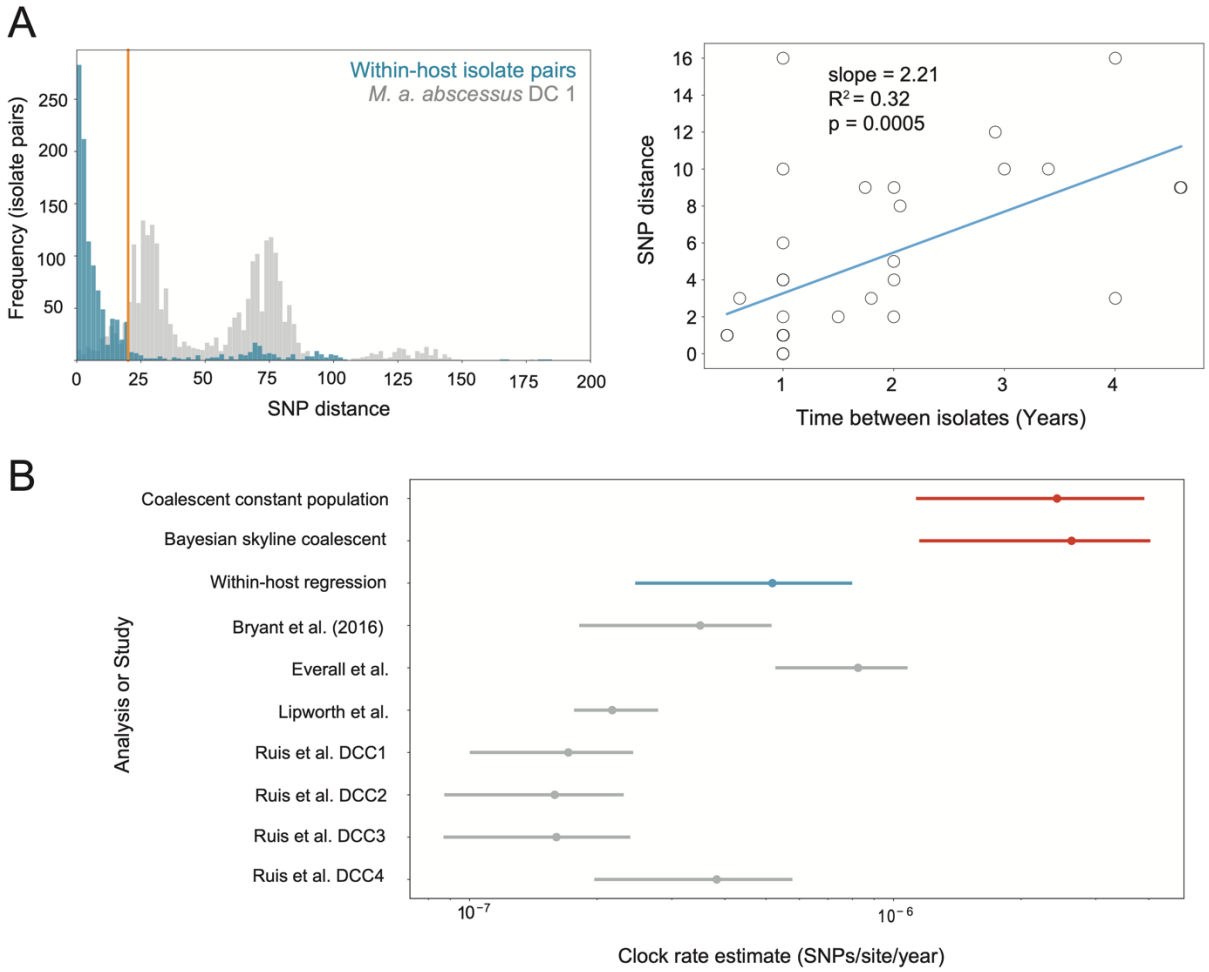

Figure 2. Longitudinally sampled within-host isolates and coalescent analysis support a slower clock rate within DCs. A) Clock rate estimation using isolate pairs sampled from the same patient over time. Left: distribution of SNP distances between all possible within- host isolate pairs compared to SNP distances between all possible isolate pairs within *M. a. abscessus* DC 1. The orange line represents the threshold of 20 SNPs used to exclude pairs representing independent infections. Right: regression of SNP distance on the time between isolates for each isolate pair. The slope of the regression line was 2.51 SNPs/year [1.24 – 3.78 95% CI], or roughly 5.93×10^{-7} SNPs/site/year [2.92×10^{-7} – 8.9×10^{-7} 95% CI]. B) UCLD clock rate estimates (dots) for the three models used in this study (two coalescent models shown in red and one regression model shown in blue) compared to mutation rate estimates from the within-host regression (blue) and published clock rates (grey). Lines represent the 95% highest posterior density interval, except in the case of the within-host regression in which case the line represents the 95% confidence interval of the regression shown in (A).

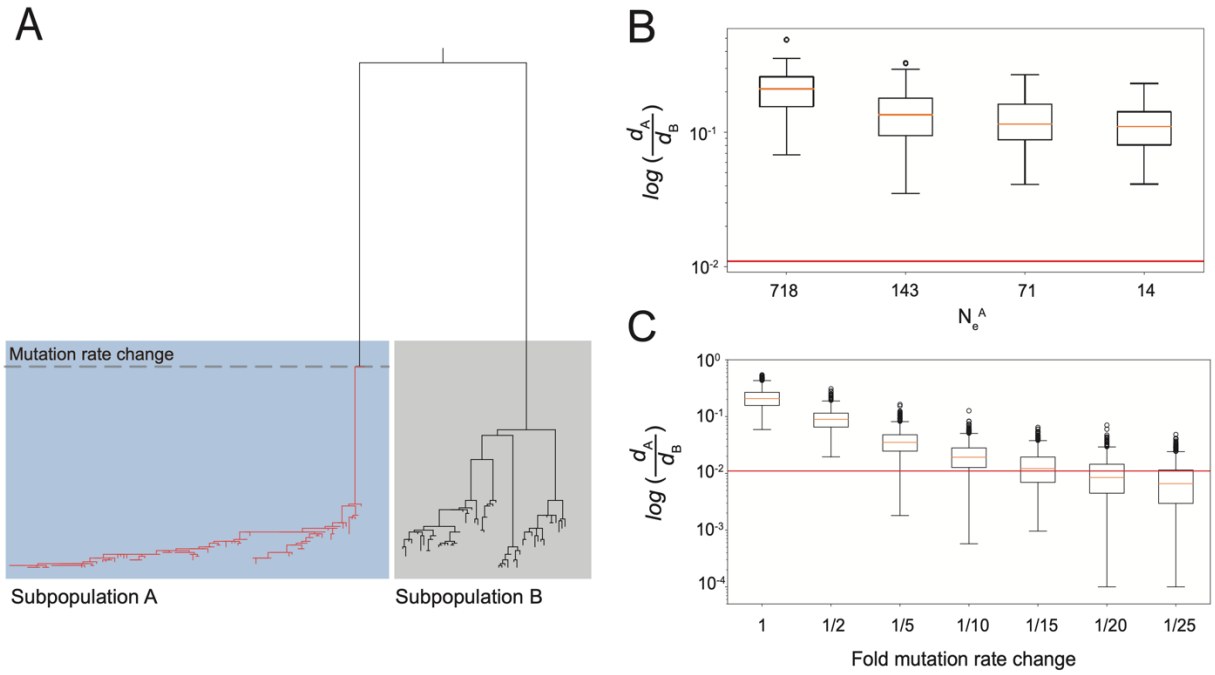

Figure 3. Simulated ancestries support a mutation rate slow-down coincident with DC emergence. A) Example neighbor joining (NJ) tree from the simulation shown in B. The number of samples and sampling dates for subpopulations A and B are drawn from real data from *M. a. abscessus* cluster 1 and from all unclustered samples, respectively. The dotted line crosses the common ancestor node for subpopulation A, and all branches descended from this node (shown here in red) are subject to the change in mutation rate. B) Boxplot showing the degree of phylogenetic clustering in subpopulation A relative to subpopulation B over a range of effective population sizes of subpopulation A (N_e^A). The simulation assumes that N_e^T=8000. C) Boxplot showing the degree of phylogenetic clustering in subpopulation A relative to subpopulation B over a range of mutation rate changes. The simulation assumes that N_e^T=8000 and N_e^A=718. In both B-C the degree of clustering is estimated with metric $\log(\frac{d_A}{d_B})$ where d_i is the mean pairwise SNP distance among all sample pairs in subpopulation i. The red lines represent the clustering metric estimated using the observed ML phylogeny. Boxes extend from the lower to upper quartile values with a line at the median. Whiskers show the range of the data.

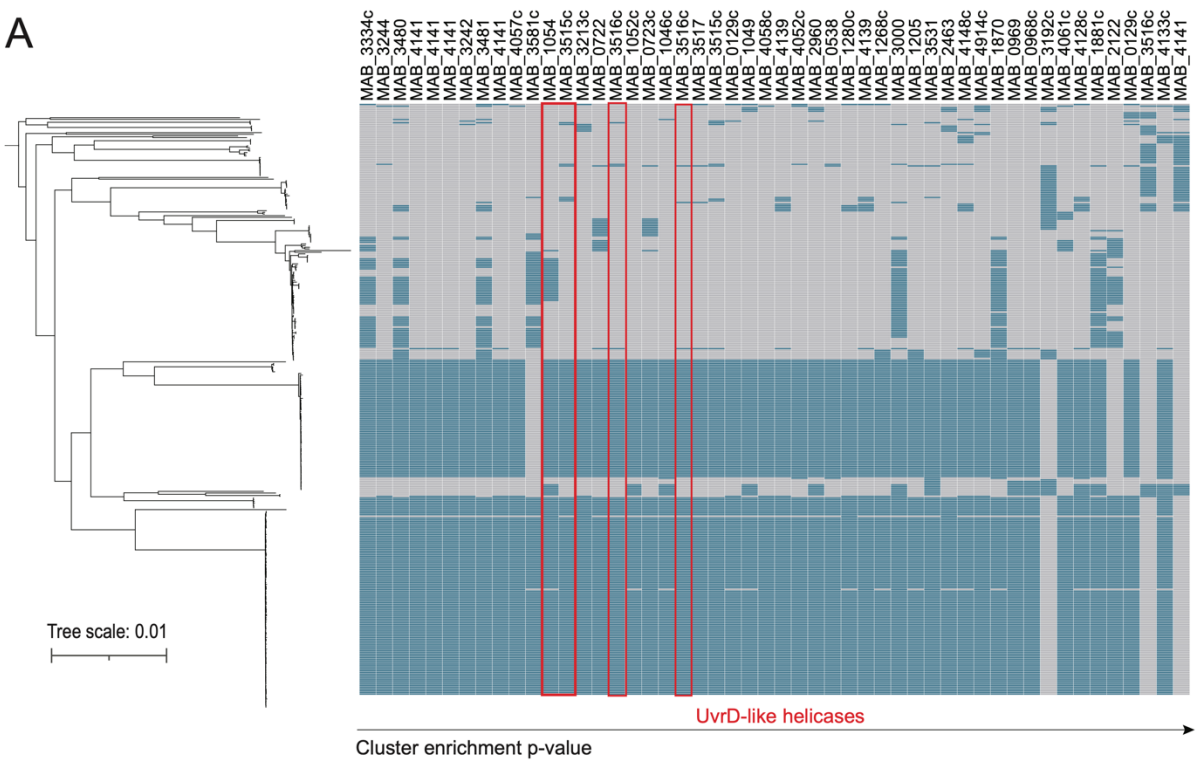
A
MAB_3334c
MAB_3244
MAB_3480
MAB_4141
MAB_4141
MAB_4141
MAB_3242
MAB_3481
MAB_4141
MAB_4057c
MAB_3581c
MAB_1054
MAB_3515c
MAB_3213c
MAB_0722
MAB_3516c
MAB_1052c
MAB_0723c
MAB_1046c
MAB_3516c
MAB_3517
MAB_3515c
MAB_0129c
MAB_1049
MAB_4058c
MAB_4139
MAB_4052c
MAB_2960
MAB_0538
MAB_1280c
MAB_4139
MAB_1268c
MAB_3000
MAB_1205
MAB_3531
MAB_2463
MAB_4148c
MAB_4914c
MAB_1870
MAB_0969
MAB_0968c
MAB_3192c
MAB_4061c
MAB_4128c
MAB_1881c
MAB_2122
MAB_0129c
MAB_3516c
MAB_4133c
MAB_4141
Tree scale: 0.01
UvrD-like helicases
Cluster enrichment p-value

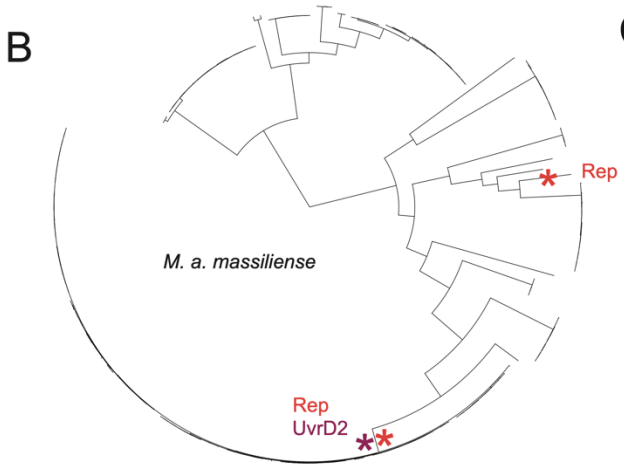
B
Rep
M. a. massiliense
Rep
UvrD2

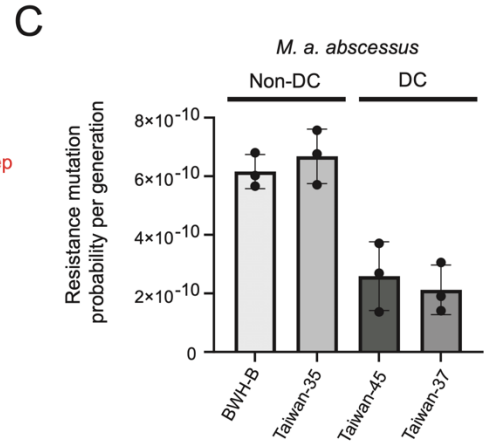
C
M. a. abscessus
Non-DC
DC
Resistance mutation probability per generation
8×10-10
6×10-10
4×10-10
2×10-10
0
BWH-B
Taiwan-35
Taiwan-45
Taiwan-37

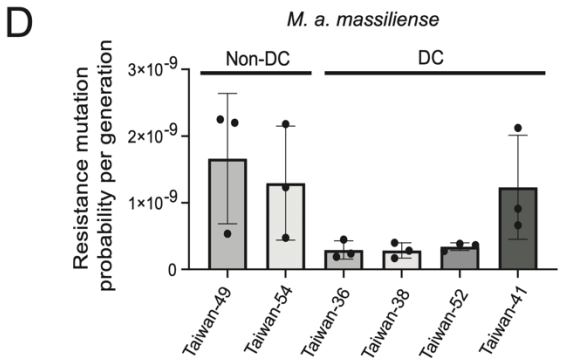
D
M. a. massiliense
Non-DC
DC
Resistance mutation probability per generation
3×10-9
2×10-9
1×10-9
0
Taiwan-49
Taiwan-54
Taiwan-36
Taiwan-38
Taiwan-52
Taiwan-41

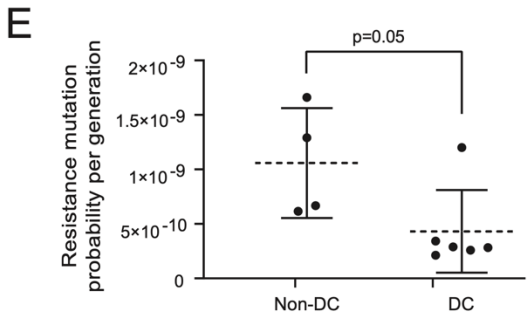
E
p=0.05
Resistance mutation probability per generation
2×10-9
1.5×10-9
1×10-9
5×10-10
0
Non-DC
DC

533

534 **Figure 4. Dominant clusters are associated with a decrease in the spontaneous mutation**
535 **rate *in vitro***. A) Subspecies phylogeny for *M. a. abscessus* (left) and corresponding heatmap
536 representing the presence of the derived allele (blue) or ancestral allele (grey) for each
537 nonsynonymous variant. Variants are ranked in ascending order by their p-value derived from
538 Fisher's tests for enrichment in the three largest clusters. The top 50 hits are shown. The genes
539 where each variant is located are denoted. B) Subspecies phylogeny for *M. a. massiliense*. The
540 branches where mutations have occurred in homologs of Rep and UvrD2 are shown with
541 asterisks. Probability of acquiring an amikacin resistance mutation per generation in C) *M. a.*
542 *abscessus* strains, D) *M. a. massiliense* strains, or D) in all strains tested that are part of a
543 dominant cluster or not. Mean +/- SD is displayed. In C-D, n=3 biological replicates. In E, each
544 point represents the average mutation probability for a single strain. p-value derived from two-
545 tailed, unpaired t-test (t=2.258, df=8).
546

547

548 **Methods**

549 Data Sources and Description: WGS data were curated from published studies[4,7,10,12,22–24] and
550 additional data were downloaded from the NCBI Sequence Read Archive (SRA). A search of
551 "abscessus" was conducted on October 4, 2019 using the filters "DNA" and "Illumina". Sequences
552 were selected that had an associated date of collection with the year at minimum. Collection dates
553 were obtained either from the literature, SRA metadata table, or provided by the authors. A
554 summary of all samples used in this study is provided in Extended Data Table 1. Raw sequencing
555 reads were downloaded using the NCBI SRA toolkit v2.9.6[25].

556

557 Quality control of Illumina reads: Reads were trimmed and filtered with trimmomatic v0.36[26]. To
558 detect contaminated samples, the mean GC content of the reads were compared to a modelled
559 normal distribution of GC content using fastqc v0.11.8[27]. If the sum of the deviations from the
560 normal distribution represented more than 30% of the reads, the sequencing run was excluded
561 from further analysis.

562

563 Subspecies assignment and genome assembly: Multiple sequencing runs corresponding to one
564 biological sample were combined into one file. Reads were then assembled *de novo* using
565 SPAdes v3.11.1[28]. Assemblies were compared to a reference sequence for each of the three

566 subspecies (Table S3) and a whole-genome based average nucleotide identity (gANI) score was
567 calculated using fastANI v1.2[29]. The resulting alignments were assigned to a subspecies based
568 on having gANI of at least 98% with exactly one reference strain. Isolates that did not have at
569 least 98% ANI with any reference strain were excluded. No isolates matched more than one
570 reference genome. After assigning isolates to a subspecies, reads were mapped to the
571 corresponding reference genome using BWA MEM v0.7.17[30]. After alignment, isolates with <80%
572 coverage of the reference genome at a depth of at least 20x or with missing data at >30% of sites
573 were excluded.
574
575 Variant calling and SNP filtering: Variants were called using Pilon v1.23[31]. We excluded
576 ambiguous calls as wells as indels and MNVs. We also excluded calls with low coverage using a
577 minimum depth of either 10% of the mean coverage, or 5, whichever was greater (default settings
578 for Pilon –mindepth). We used bcftools v1.10.2[32] to exclude calls with mapping quality or base
579 quality scores < 20.
580
581 Core genome inference: Unlike the professional mycobacterial pathogens *M. tuberculosis* or *M.*
582 *leprae*, which have small accessory genomes, *M. abscessus* has a large, open accessory
583 genome[33]. To define the core genome for phylogenetic analysis and to exclude loci that are highly
584 divergent from the reference sequence, we masked all loci for downstream analysis where read
585 depth was <20x in more than 5% of the isolates in our sample set. The remaining loci were
586 compared to an estimate of the core genome calculated by Roary[34], and the two methods yielded
587 nearly identical results. We further excluded regions with average mapping quality scores or
588 average based quality scores <20. Finally, we used GenMap v1.1[35] to calculate mappability
589 scores across each reference genome as defined in reference[36]. We then calculated a mappability
590 pileup score for each base position as described in reference[37] and excluded loci where the
591 mappability pileup score was <95% from downstream analysis. In total, we excluded 14.4%,

592 13.5%, and 15.1% of the *M. a. abscessus*, *M. a. massiliense*, and *M. a. bolletii* reference genome
593 length, respectively.
594
595 Phylogenetic tree inference: A full-length sequence alignment was created using a custom script,
596 masking loci excluded by our filtering criteria described above. Gubbins v2.4.1[38] was used to
597 predict and mask regions of variation produced by recombination from the full-length alignment.
598 A recombination-free SNP alignment generated by Gubbins was then used to build a phylogeny
599 for each subspecies using IQ-TREE v1.6.12[39], using the ModelFinder Plus (-mfp) option and 1000
600 bootstrap replicates. Clusters were defined as previously described[4] using a one-dimensional
601 scanning statistic to identify clades with a distribution of branch lengths that is shorter than the
602 distribution of branch lengths in the rest of the tree[41].
603
604 Coalescent analysis: Temporal signal was assessed using root-to-tip regression. In both *M. a.*
605 *abscessus* and *M. a. massiliense* subspecies trees and all three major clusters, a slightly negative
606 slope was observed, indicated lack of temporal signal. We recognized that the high degree of
607 clustering and short time span over which the clustered isolates were sampled may confound the
608 genetic temporal signal. To address this, we pruned the trees down to taxa that preserved 95%
609 of the relative tree length (RTL) of the original trees using Treemmer v0.3[42]. A threshold of 95%
610 eliminated most of the dense clustering, but preserved the long branches of the original tree
611 (Figure 2B, Figure S2B). Using the pruned tree, we observed evidence of temporal signal in the
612 MAB subspecies by regressing the root-to-tip distance for each sample against the date of
613 collection. The linear regression was performed using the statsmodels package and the Pearson
614 correlation coefficient was calculated using the pingouin package in Python. We generated a SNP
615 alignment including only the taxa present in the pruned *M. a. abscessus* tree and used this as
616 input for coalescent analysis using BEAST v2.6.3[42]. ModelTest-NG v0.1.6 [43] was used to select
617 the site model GTR+4. MegaX[44] was used to perform a maximum likelihood test to determine that

618 a relaxed clock model is best suited for our data. This choice was confirmed using the nested
619 sampling algorithm to compare marginal likelihoods for a strict v. relaxed clock model. We then
620 used nested sampling to compare various tree priors. We used Bayesian Evaluation of Temporal
621 Signal (BETS) to confirm the presence of temporal signal by comparing marginal likelihoods when
622 the tip dates were used to those when all samples were assumed to be isochronous (Table S4).
623 Based on marginal likelihood values, we ran both a coalescent constant population model and a
624 Bayesian skyline coalescent model, assuming a relaxed clock and including the sampling dates
625 for both models. We used the ML phylogeny of the pruned dataset as a starting tree. For each
626 model we ran two independent chains for at least 100 million states to ensure convergence.
627 To test the effects of different recombination search procedures, we used Gubins v3.2.1
628 using 1) the default parameters and 2) more stringent search parameters by: decreasing the
629 minimum number of SNPs to call a recombination to 2, increasing the significance threshold to
630 p=0.10, and raising the trimming ratio to 1.5 to disfavor trimming of recombination edges. We also
631 implemented recombination search using an alternative algorithm, ClonalFrameML[45]. We then
632 used BEAST to estimate clock rates using each alignment, assuming a constant population tree
633 prior (Figure S2B). To test the effects of which isolates are sampled by Treemmer, we ran
634 Treemmer 10 times to obtain 10 independent samples. We then repeated our analysis using
635 BEAST, again assuming a constant population tree prior (Figure S2C).
636
637 Phylogenetic dating: To attempt to date the full MAB phylogeny, we ran both coalescent constant
638 population and Bayesian skyline coalescent models assuming a relaxed clock without sampling
639 dates. We set the mean UCLD clock rate to the values estimated from our coalescent analysis of
640 the pruned tree. We ran each chain for at least 100 million states.
641
642 Estimation of mutation rate within-host: We identified 90 patients with two or more *M. a. abscessus*
643 isolates. Because coinfection with multiple *M. abscessus* clones is common in cystic fibrosis

644 patients, we first sought to exclude any isolate pairs that represented distinct clonal infections.
645 We selected a threshold of 20 SNPs by comparing the distribution of all possible within-host
646 isolate pairs to the distribution of pairwise SNP distances within *Mab* clusters. We further excluded
647 any isolates where >20% of the genome is predicted to be rearranged by recombination. For the
648 remaining isolate pairs we regressed the pairwise SNP distance between the first and last isolates
649 sampled from each patient on the time between the collection of each sample. The linear
650 regression was performed using the Python statsmodels package v0.12.2. The slope of the
651 regression line was used as an estimate of the number of SNPs accumulated over time.
652 Ancestry simulations: We used msprime v1.0.2[46] to simulate ancestries to model two
653 subpopulations: (1) a "clustered" subpopulation (A) and (2) an "unclustered" subpopulation (B).
654 We assumed a constant population size and initially set the total effective population size (N_e) to
655 8000, the N_e estimated in our coalescent analysis of the pruned *Mab* tree. We chose a range of
656 realistic N_e for subpopulation A, N_e^A by running a separate coalescent analysis of *M. a. abscessus*
657 cluster 1 using BEAST, assuming a constant population size, relaxed clock, and a range of UCLD
658 clock rates spanning 1.7×10^{-7} SNPs/site/year, as previously reported for this cluster by Ruis et al.
659 (2021) to 8.5×10^{-6} SNPs/site/year, a value well above the 95% HPD interval for our estimate of
660 the clock rate in the pruned tree (Table S5). We assumed the N_e of subpopulation B to be: N_e^B =
661 N_e^{total}-N_e^A. The number of samples and sampling dates supplied to the model for subpopulations
662 A and B are drawn from the true values for *Mab* cluster 1 and from all "unclustered" isolates in
663 the tree, respectively. We assumed an initial mutation rate of 1×10^{-9} mutations/generation with a
664 sequence length of 5Mb and a divergence time of 30,000 generations between subpopulations A
665 and B. We also assumed the nucleotide subsitution model estimated using BEAST.
666 We first simulated a scenario where the mutation rate remains constant, varying N_e^A over
667 the range shown in Table S5. For each simulated ancestry we overlaid mutation events, supplying
668 the model with a starting substitution rate of 1×10^{-9} mutations/generation, a nucleotide substitution
669 model estimated using BEAST, and a sequence length of 5Mb. We then extracted the simulated

670 genotypes and constructed a neighbor joining (NJ) tree using the Phylo module of the Python
671 package biopython v1.79. The NJ tree was used to exclude any simulations where the two
672 subpopulations did not exhibit reciprocal monophyly. We used the extracted genotypes to
673 estimate the degree of clustering in each tree by comparing the mean pairwise SNP distance in
674 subpopulation A (d_A) to the mean pairwise SNP distance in subpopulation B (d_B). For each
675 simulated condition we performed 1000 replicates. To simulate ancestries with a mutation rate
676 change, we repeated the above procedure conservatively assuming N_e^A = 718. We modeled a
677 per-generation mutation rate change starting at the common ancestor node for subpopulation A
678 and ranging from 1-fold (no change) to 1/25-fold spanning a range of reasonable rate changes
679 based on the range of clock rate estimates observed in this study and reported in the literature
680 (Figure 2B). For all simulated conditions, we the simulation over a range of values for N_e^{total}
681 spanning the 95% HPD intervals for the N_e estimates using the Treemmer tree under both the
682 constant coalescent and coalescent skyline tree priors.
683
684 Scan for variants enriched in clinically successful clades: To search for variants associated with
685 DCs, we first inferred the number of independent arisals in the MAB phylogeny for each SNP
686 using SNPPar v1.0[46]. Briefly, SNPPar uses TreeTime to perform an ancestral sequence
687 reconstruction at each node, then infers mutation events arising on each branch of the tree. We
688 quantified the number of independent mutation events for each SNP. We considered only
689 mutation events where the derived call was the minor allele and the ancestral call was the major
690 allele. Because of the extreme phylogenetic clustering in *Mab*, we defined the major and minor
691 alleles using the pruned alignment generated by Treemmer. For all homoplasic SNPs (occurring
692 two or more times independently in the tree), we used Fisher's exact test to quantify the
693 enrichment of that variant within phylogenetic clusters and reported FDR-adjusted p-values to
694 correct for multiple testing. We conducted two separate analyses: a) focusing on the three largest
695 clusters in the *M. A. abscessus* tree (described in the main text), and b) considering all clusters

696 identified by this approach. In each case we obtained similar results. For both analyses, full lists
697 of variants ranked by their enrichment scores are provided in Supplementary Data. For each
698 variant reported in Table 2, we manually examined SNPPar output to confirm that the variant was
699 acquired independently along branches ancestral to at least 2 separate clusters. We also used
700 SNPPar to identify all mutation events occurring on the branch ancestral to *M. a. massiliense*
701 cluster 1.
702
703 *M. abscessus* culture: *M. abscessus* clinical isolates used for fluctuation assays were isolated
704 from patients in Taiwan and in Boston, MA, USA. All *M. abscessus* strains were cultured in
705 Middlebrook 7H9 broth (271310, BD Diagnostics, Franklin Lakes, NJ, USA) with 0.2% (v/v)
706 glycerol, 0.05% (v/v) Tween-80 (P1754, Sigma-Aldrich, St. Louis, MO, USA), and 10% (v/v)
707 OADC (90000-614, VWR, Radnor, PA, USA). Proliferation rates were determined by inoculating
708 5 mL media with 500,000 colony forming units (cfu), then measuring OD600 at 24 and 48 hours
709 post-inoculation. Proliferation rate was calculated as follows: proliferation rate in doublings per
710 day = $\log_2$(OD600 at 48 hours / OD600 at 24 hours).
711
712 Fluctuation Assay: Fluctuation assays were performed as described previously[17] with adaptations
713 for *M. abscessus*. *M. abscessus* strains were grown to saturation, then diluted to an OD600 <
714 0.01 and grown overnight until cultures reached an OD600 = 0.6-0.8. These cultures were used
715 for fluctuation assays as well as determination of baseline amikacin sensitivity. Baseline amikacin
716 sensitivity was tested by spreading dilutions of 10 million, 100 million, or 1 billion cfu on agar 7H10
717 (262710, BD Diagnostics) + OADC (90000-614, VWR) + 300 µg/mL amikacin sulfate (A2324,
718 Sigma-Aldrich) plates. For fluctuation assays, 5000 cfu were plated in 1 mL media in each of 21
719 wells of a 24-well culture plate (10861-558, VWR), and initial cultures were plated for cfu on 7H10
720 + OADC to confirm number of cells in initial culture. 24-well plates were incubated shaking at 150
721 rpm for 6 days at 37°C. 18 wells of each strain were plated onto 6-well plates containing 5 mL

722 7H10 agar + OADC + 300 µg/mL amikacin sulfate in each well. Amikacin was used as the
723 antibiotic selection for the assay because all tested strains had low baseline resistance (Table
724 S8), which is required for the validity of the fluctuation assay. The remaining 3 wells from each
725 strain were diluted and plated on 7H10 + OADC plates to enumerate average final cfu. Colonies
726 on all agar plates were counted after 5 days incubation at 37°C. Mutation rate per generation per
727 total number of bases that can be mutated to confer amikacin resistance was calculated using
728 the Shinyflan application for the flan R package v0.9[17] using the Maximum Likelihood estimation
729 method, assumption of unknown fitness effects of mutations, the Exponential (LD model)
730 distribution of mutant lifetime, and a Winsor parameter of 1024. One strain (BWH-E) was excluded
731 from analysis due to highly variable results across replicates (Figure S6B). Mutation rates in
732 clustered and unclustered samples were compared using a two-tailed, unpaired t-test with
733 GraphPad Prism v9.3.1.
734
735 **Code Availability**
736 Notebooks, snakemake piplines, custom scripts, conda environments, and BEAST XML files are
737 available at: https://github.com/nicolettacommins/mab_mutation_rates_2022.
738
739 **Data Availability**
740 Accession IDs for all publicly available data used in this study are available in the
741 supplementary file: mabsc_all_sample_metadata.csv.
742
743
744
745
746
747

753 **References**

754 1. Adjemian, J., Olivier, K. N. & Prevots, D. R. Epidemiology of Pulmonary Nontuberculous
755 Mycobacterial Sputum Positivity in Patients with Cystic Fibrosis in the United States, 2010-
756 2014. *Ann. Am. Thorac. Soc.* **15**, 817–826 (2018).

757 2. Lee, M.-R. *et al.* Mycobacterium abscessus Complex Infections in Humans. *Emerg. Infect.*
758 *Dis.* **21**, 1638–1646 (2015).

759 3. Nessar, R., Cambau, E., Reyrat, J. M., Murray, A. & Gicquel, B. Mycobacterium abscessus:
760 a new antibiotic nightmare. *J. Antimicrob. Chemother.* **67**, 810–818 (2012).

761 4. Bryant, J. M. *et al.* Emergence and spread of a human-transmissible multidrug-resistant
762 nontuberculous mycobacterium. *Science* **354**, 751–757 (2016).

763 5. Bange, F. C., Brown, B. A., Smaczny, C., Wallace, R. J., Jr & Böttger, E. C. Lack of
764 transmission of mycobacterium abscessus among patients with cystic fibrosis attending a
765 single clinic. *Clin. Infect. Dis.* **32**, 1648–1650 (2001).

766 6. Olivier, K. N. *et al.* Nontuberculous mycobacteria. I: multicenter prevalence study in cystic
767 fibrosis. *Am. J. Respir. Crit. Care Med.* **167**, 828–834 (2003).

768 7. Doyle, R. M. *et al.* Cross-transmission is not the source of new Mycobacterium abscessus
769 infections in a multi-centre cohort of cystic fibrosis patients. *Clin. Infect. Dis.* (2019)
770 doi:10.1093/cid/ciz526.

771 8. Sermet-Gaudelus, I. *et al.* Mycobacterium abscessus and children with cystic fibrosis. *Emerg.*
772 *Infect. Dis.* **9**, 1587–1591 (2003).

773 9. Lipworth, S. *et al.* Epidemiology of Mycobacterium abscessus in England: an observational
774 study. *The Lancet Microbe* (2021) doi:10.1016/S2666-5247(21)00128-2.

775 10. Harris, K. A. *et al.* Whole-genome sequencing and epidemiological analysis do not provide
776 evidence for cross-transmission of mycobacterium abscessus in a cohort of pediatric cystic
777 fibrosis patients. *Clin. Infect. Dis.* **60**, 1007–1016 (2015).

778 11. Tortoli, E. *et al.* Mycobacterium abscessus in patients with cystic fibrosis: low impact of inter-
779 human transmission in Italy. *Eur. Respir. J.* **50**, (2017).
780 12. Everall, I. *et al.* Genomic epidemiology of a national outbreak of post-surgical Mycobacterium
781 abscessus wound infections in Brazil. *Microb Genom* **3**, e000111 (2017).
782 13. Ruis, C. *et al.* Dissemination of Mycobacterium abscessus via global transmission networks.
783 *Nature Microbiology* 1–10 (2021) doi:10.1038/s41564-021-00963-3.
784 14. Bouckaert, R. *et al.* BEAST 2.5: An advanced software platform for Bayesian evolutionary
785 analysis. *PLoS Comput. Biol.* **15**, e1006650 (2019).
786 15. Houghton, J. *et al.* Important role for Mycobacterium tuberculosis UvrD1 in pathogenesis and
787 persistence apart from its function in nucleotide excision repair. *J. Bacteriol.* **194**, 2916–2923
788 (2012).
789 16. Sinha, K. M., Unciuleac, M.-C., Glickman, M. S. & Shuman, S. AdnAB: a new DSB-resecting
790 motor-nuclease from mycobacteria. *Genes Dev.* **23**, 1423–1437 (2009).
791 17. Krašovec, R. *et al.* Measuring Microbial Mutation Rates with the Fluctuation Assay. *J. Vis.*
792 *Exp.* (2019) doi:10.3791/60406.
793 18. Ho, S. Y. W., Shapiro, B., Phillips, M. J., Cooper, A. & Drummond, A. J. Evidence for time
794 dependency of molecular rate estimates. *Syst. Biol.* **56**, 515–522 (2007).
795 19. Huffnagle, G. B., Dickson, R. P. & Lukacs, N. W. The respiratory tract microbiome and lung
796 inflammation: a two-way street. *Mucosal Immunol.* **10**, 299–306 (2017).
797 20. Bryant, J. M. *et al.* Stepwise pathogenic evolution of Mycobacterium abscessus. *Science*
798 **372**, (2021).
799 21. Curti, E., Smerdon, S. J. & Davis, E. O. Characterization of the helicase activity and substrate
800 specificity of Mycobacterium tuberculosis UvrD. *J. Bacteriol.* **189**, 1542–1555 (2007).
801 22. Bryant, J. M. *et al.* Whole-genome sequencing to identify transmission of Mycobacterium
802 abscessus between patients with cystic fibrosis: a retrospective cohort study. *Lancet* **381**,
803 1551–1560 (2013).

804 23. Hasan, N. A. *et al.* Population Genomics of Nontuberculous Mycobacteria Recovered from
805 United States Cystic Fibrosis Patients. *bioRxiv* 663559 (2019) doi:10.1101/663559.
806 24. Shaw, L. P. *et al.* Children with cystic fibrosis are infected with multiple subpopulations of
807 Mycobacterium abscessus with different antimicrobial resistance profiles. *Clin. Infect. Dis.*
808 (2019) doi:10.1093/cid/ciz069.
809 25. Download : Software : Sequence Read Archive : NCBI/NLM/NIH.
810 https://trace.ncbi.nlm.nih.gov/Traces/sra/sra.cgi?view=software.
811 26. Bolger, A. M., Lohse, M. & Usadel, B. Trimmomatic: a flexible trimmer for Illumina sequence
812 data. *Bioinformatics* **30**, 2114–2120 (2014).
813 27. Babraham Bioinformatics - FastQC A Quality Control tool for High Throughput Sequence
814 Data. https://www.bioinformatics.babraham.ac.uk/projects/fastqc/.
815 28. Prjibelski, A., Antipov, D., Meleshko, D., Lapidus, A. & Korobeynikov, A. Using SPAdes De
816 Novo Assembler. *Curr. Protoc. Bioinformatics* **70**, e102 (2020).
817 29. Jain, C., Rodriguez-R, L. M., Phillippy, A. M., Konstantinidis, K. T. & Aluru, S. High throughput
818 ANI analysis of 90K prokaryotic genomes reveals clear species boundaries. *Nat. Commun.*
819 **9**, 5114 (2018).
820 30. Li, H. Aligning sequence reads, clone sequences and assembly contigs with BWA-MEM.
821 *arXiv [q-bio.GN]* (2013).
822 31. Walker, B. J. *et al.* Pilon: an integrated tool for comprehensive microbial variant detection
823 and genome assembly improvement. *PLoS One* **9**, e112963 (2014).
824 32. Li, H. A statistical framework for SNP calling, mutation discovery, association mapping and
825 population genetical parameter estimation from sequencing data. *Bioinformatics* **27**, 2987–
826 2993 (2011).
827 33. Choo, S. W. *et al.* Genomic reconnaissance of clinical isolates of emerging human pathogen
828 Mycobacterium abscessus reveals high evolutionary potential. *Sci. Rep.* **4**, 4061 (2014).

829 34. Page, A. J. *et al.* Roary: rapid large-scale prokaryote pan genome analysis. *Bioinformatics*
830 **31**, 3691–3693 (2015).
831 35. Pockrandt, C., Alzamel, M., Iliopoulos, C. S. & Reinert, K. GenMap: ultra-fast computation of
832 genome mappability. *Bioinformatics* **36**, 3687–3692 (2020).
833 36. Derrien, T. *et al.* Fast computation and applications of genome mappability. *PLoS One* **7**,
834 e30377 (2012).
835 37. Marin, M. *et al.* Benchmarking the empirical accuracy of short-read sequencing across the
836 M. tuberculosis genome. *Bioinformatics* (2022) doi:10.1093/bioinformatics/btac023.
837 38. Croucher, N. J. *et al.* Rapid phylogenetic analysis of large samples of recombinant bacterial
838 whole genome sequences using Gubbins. *Nucleic Acids Res.* **43**, e15 (2015).
839 39. Minh, B. Q. *et al.* IQ-TREE 2: New Models and Efficient Methods for Phylogenetic Inference
840 in the Genomic Era. *Mol. Biol. Evol.* **37**, 1530–1534 (2020).
841 40. Harris, S. TreeGubbins. Preprint at https://github.com/simonrharris/tree_gubbins (2016).
842 41. Menardo, F. *et al.* Treemmer: a tool to reduce large phylogenetic datasets with minimal loss
843 of diversity. *BMC Bioinformatics* **19**, 164 (2018).
844 42. Darriba, D. *et al.* ModelTest-NG: A New and Scalable Tool for the Selection of DNA and
845 Protein Evolutionary Models. *Mol. Biol. Evol.* **37**, 291–294 (2020).
846 43. Kumar, S., Stecher, G., Li, M., Knyaz, C. & Tamura, K. MEGA X: Molecular Evolutionary
847 Genetics Analysis across Computing Platforms. *Mol. Biol. Evol.* **35**, 1547–1549 (2018).
848 44. Didelot, X. & Wilson, D. J. ClonalFrameML: efficient inference of recombination in whole
849 bacterial genomes. *PLoS Comput. Biol.* **11**, e1004041 (2015).
850 45. Kelleher, J. & Lohse, K. Coalescent Simulation with msprime. in *Statistical Population*
851 *Genomics* (ed. Dutheil, J. Y.) 191–230 (Springer US, 2020). doi:10.1007/978-1-0716-0199-
852 0_9.

46. Edwards, D. J., Duchêne, S., Pope, B. & Holt, K. E. SNPPar: identifying convergent evolution and other homoplasies from microbial whole-genome alignments. *bioRxiv* 2020.07.08.194480 (2020) doi:10.1101/2020.07.08.194480.